Supplementary Information (SI) for Nanoscale.

"Supporting Information"

Piezo-phototronic flexible photodetectors based on spatially aligned InN nanowires embedded in graphene channel

Seunghwan Jhee[a], Jaehyeok Shin[a], Sumin Kang[a], Yumin Lee[a], Jaemin Lee[a], Nam-In Kim[b], Jae-Hyun Ryou[b, c], Namkoo Ha[d], Ducklae Kim[d], Sangmi Na[d] and Jin Soo Kim*[a]

[a]Department of Electronic and Information Materials Engineering, Division of Advanced Materials Engineering, and Research Center of Advanced Materials Development, and Research Institute of Materials and Energy Science, Jeonbuk National University, Jeonju 54896, Republic of Korea
[b]Department of Mechanical and Aerospace Engineering, Texas Center for Superconductivity at UH, Advanced Manufacturing Institute, University of Houston, Houston, Texas 77204-4006, USA
[c]Department of Electrical and Computer Engineering, Materials Science and Engineering Program, University of Houston, Houston, Texas 77204, USA
[d]EO/IR Systems R&D, LIG Nex1, Seongnam 13494, Republic of Korea

*Corresponding author: (e-mail) kjinsoo@jbnu.ac.kr; (Tel.) +82-63-270-2291; (Fax) +82-63-270-2305

FE-SEM images of PDs with different NW alignments fabricated on graphene/IDT

Fig. S1a presents conceptual schematics of the three PD configurations— random (RAND-PD), perpendicular (PERP-PD), and parallel (PARA-PD)—which differ in terms of the orientation of the InN NWs with respect to the bending direction**.** Fig. S1b shows FE-SEM images of the InN NWs dispersed on graphene/IDT, which are randomly distributed or aligned perpendicular or parallel to the bending direction of the device. Fig. S1c shows the low-magnified plan-view FE-SEM images of the PARA-PD with the graphene/IDT structure, illustrating the overall device geometry. The IDT spacing is 50 µm, and the channel width is 100 µm.

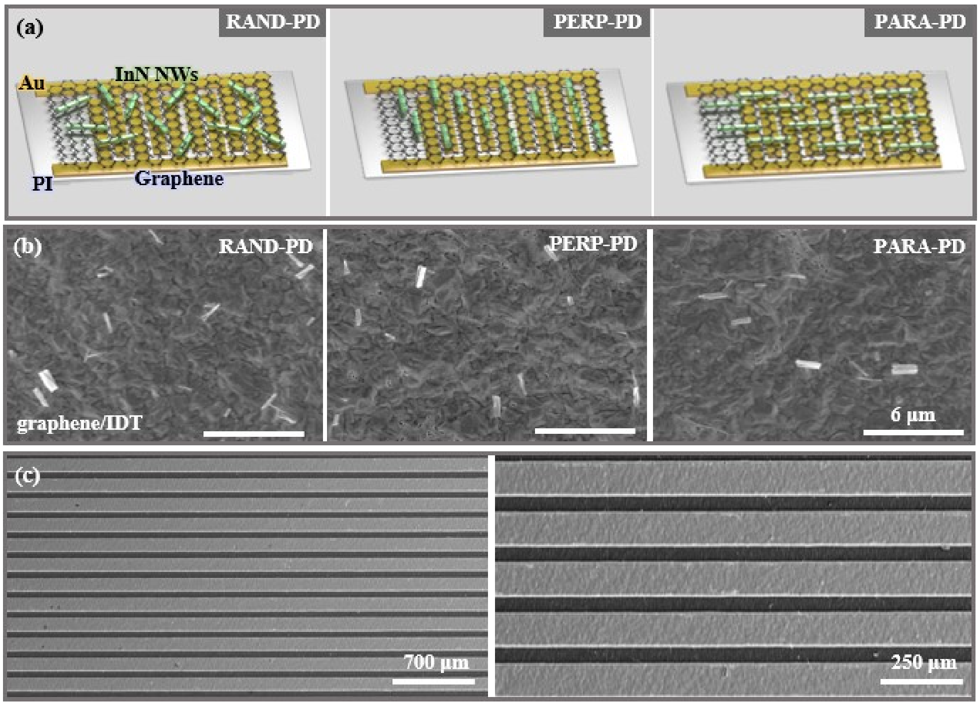

Fig. S1 (a) Conceptual schematics of the PDs with different NW orientations relative to the bending direction: RAND-PD, PERP-PD, and PARA-PD. (b) Plan-view FE-SEM images of InN NWs in different orientations. (c) Low-magnified plan-view FE-SEM images of PARA-PD with the graphene/IDT structure.

Normalized dark current variation under bending

Fig. S2 shows the dark current of the PARA-PD measured under initial and bending (2.92% strain) conditions in the absence of illumination. The normalized dark current variation ($\Delta I/I_0$) was calculated to be 0.97%, confirming that the strain-induced modulation of the dark current is negligible.

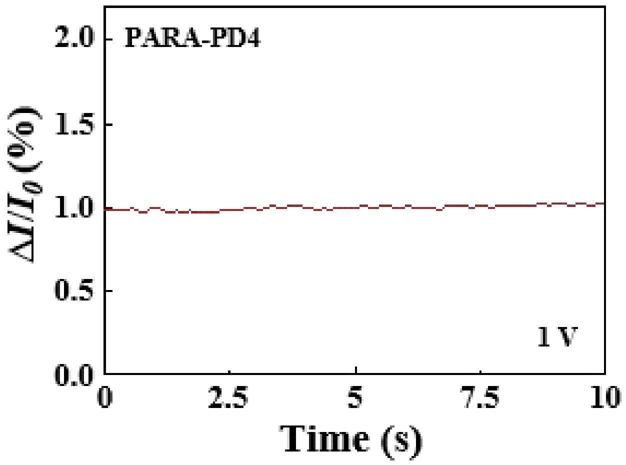

Fig. S2 Normalized dark current variation ($\Delta I/I_0$) under initial and bending conditions.

Electrical characteristics of graphene/IDT devices with and without InN NWs under initial and bending conditions

Fig. S3a shows the electrical characteristics of the graphene/IDT device without InN NWs under initial and bending conditions. The measurements were performed under an illumination intensity of 70 mW/cm^2 at an applied bias of 1 V. The photocurrents were measured to be 0.08 mA in the initial state and 0.09 mA under bending conditions. The dark current increased by 0.86% after bending. Fig. S3b shows the photocurrent measured under bending conditions for the graphene/IDT structure with and without InN NWs. Under bending, the photocurrent was 1.25 mA for the device with InN NWs (PARA-PD), whereas it was 0.09 mA for the device without InN NWs.

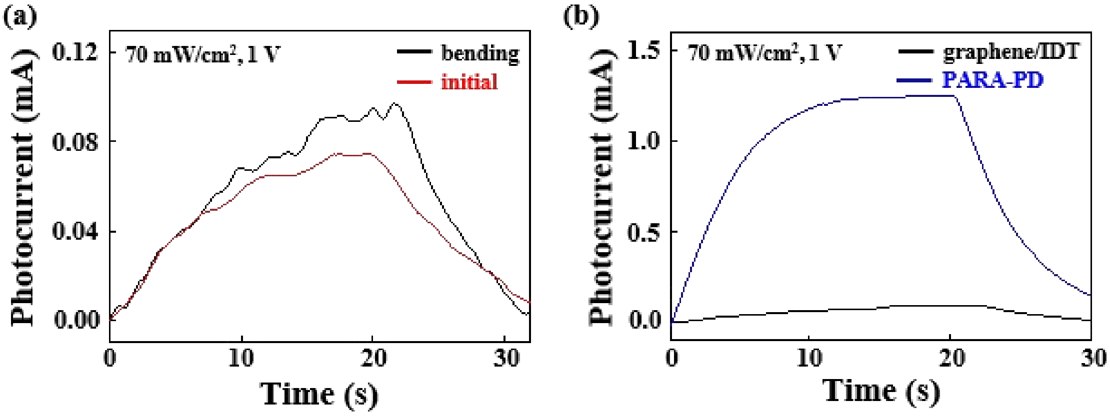

Fig. S3 (a) Photocurrents of the graphene/IDT device without InN NWs under initial and bending conditions. (b) Photocurrents of the graphene/IDT device with and without InN NWs under bending conditions.

Calculation of the piezoelectric potential in the InN NW

The piezoelectric potential inside the InN NW was calculated using the linear piezoelectric constitutive relations in the stress–charge form. The mechanical equilibrium in the NW is governed by:

$$\nabla \cdot \sigma = 0 \tag{1}$$

where σ is the stress tensor.

The electrostatic field satisfies Gauss's law,

$$\nabla \cdot D = \rho_v \tag{2}$$

and the electric field is defined as

$$E =- \nabla V, \tag{3}$$

where D is the electric displacement field, E is the electric field, V is the electric potential, and ρ_v represents the free charge density. In the present simulation, no free charge density was introduced ($\rho_v = 0$).

The electromechanical coupling of the piezoelectric material is described by

$$\sigma = c_E S - e^T E, \tag{4}$$

$$D = eS + \varepsilon_S E, \tag{5}$$

where S is the strain tensor, c_E is the elastic stiffness tensor, e is the piezoelectric stress constant matrix, and ε_S is the permittivity tensor.

The mechanical boundary condition was imposed by fixing one end of the NW such that

$$u = 0 \tag{6}$$

while a force of 0.08 μN was applied at the opposite end. Electrically, one boundary was set to

$$V = 0 \tag{7}$$

and all remaining boundaries satisfied

$$n \cdot D = 0 \tag{8}$$

These coupled equations were solved simultaneously to obtain the piezoelectric potential distribution in the InN NW. The simulations were carried out using COMSOL Multiphysics based on the standard linear piezoelectric formulation implemented in the structural mechanics and electrostatics modules. The elastic stiffness constants, piezoelectric stress coefficients, and dielectric permittivities used in the simulation were adopted from previous report.[1] The elastic stiffness tensor components (GPa) were:

$C_{11} = 223, \quad C_{12} = 115, \quad C_{13} = 92,$

$C_{33} = 224, \quad C_{44} = 48, \quad C_{66} = 54.$

The piezoelectric stress constants were:

$e_{31} = -0.57 C/m^2, \quad e_{33} = 1.32\ C/m^2, \quad e_{15} = -0.29\ C/m^2.$

The numerical simulation was performed to qualitatively illustrate the strain-induced piezoelectric potential distribution rather than to quantitatively reproduce the exact experimental strain magnitude.

Bending deformation and simulation model of the InN NW

Fig. S4 illustrates the bending deformation behavior of the InN NW under an applied force, along with the simulation model and boundary conditions used in this study. In the simulation, one end of the NW was fixed (u = 0), while the force of 0.08 μN was applied to induce bending deformation. This configuration generates mechanical strain within the NW, leading to the piezoelectric response.

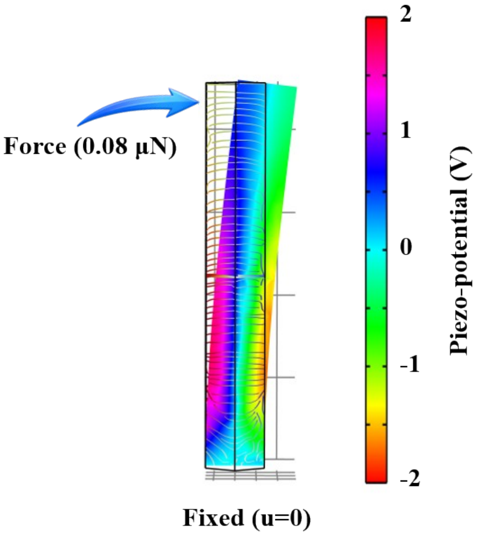

Fig. S4 Illustration of bending deformation of an InN NW under a force.

Photocurrent of RAND-PD and PERP-PD as a function of applied strain

Fig. S5 shows the photocurrent of the (a) RAND-PD and (b) PERP-PD as a function of applied strain. The measurements were performed under an illumination intensity of 70 mW/cm² at an applied bias of 1 V. For the RAND-PD, the photocurrent was measured to be 0.58 mA in the unstrained state and increased to 0.77 mA at a strain level of 2.92. For the PERP-PD, the photocurrent increased from 0.56 mA to 0.65 mA under the same strain condition.

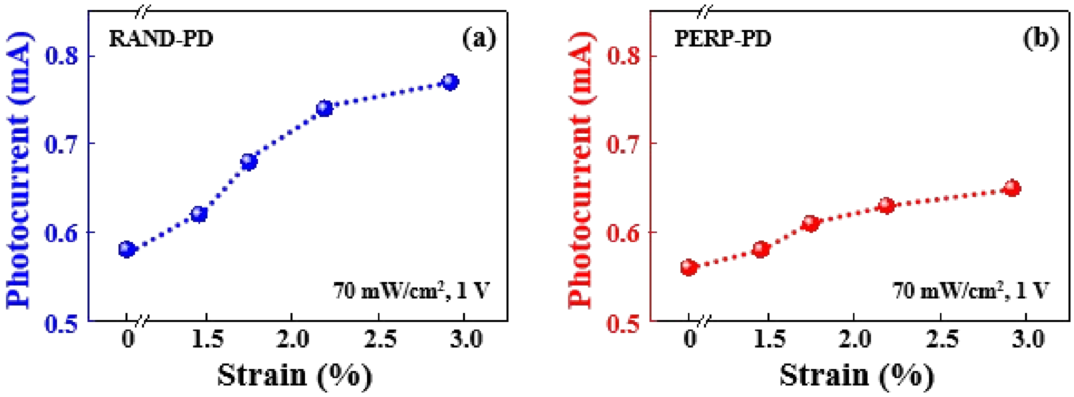

Fig. S5 Summary on the strain-dependent photocurrents of (a) RAND-PD and (b) PERP-PD.

Temporal response characteristics of PARA-PD under light illumination.

Fig. S6 shows the temporal response of the PARA-PD under light illumination. The device has a rise time of 7.51 s and a decay time of 9.55 s, where the rise and decay times were defined as the durations required for the current to change between 10% and 90% of the steady-state photocurrent. Similar time scales have been reported in graphene-based hybrid PDs governed by photoconductive or photogating mechanisms.[2, 3] In the present structure, graphene enables efficient lateral carrier extraction owing to its high mobility. Nevertheless, some photogenerated carriers may be temporarily trapped at the mixed-dimensional NW/graphene interface, which can extend the effective carrier lifetime and slightly delay the recovery process.[4]

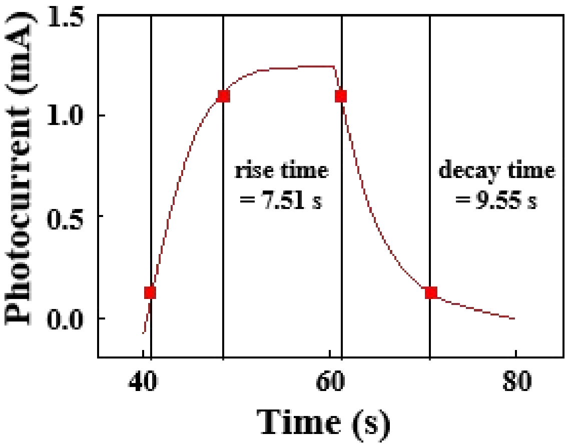

Fig. S6 Rise and decay times of PARA-PD4.

Time-dependent Raman analysis of the graphene channel

Fig. S7 shows the Raman spectra of the graphene channel acquired immediately after fabrication and after 28 days of storage. The spectra exhibit the G (~1580 cm^{-1}) and 2D (~2680 cm^{-1}) modes of graphene, with no discernible enhancement of the defect-related D band after storage. Furthermore, the peak positions and line shapes remain essentially unchanged, indicating that no additional defects or oxidation were introduced during the storage period. [5, 6]

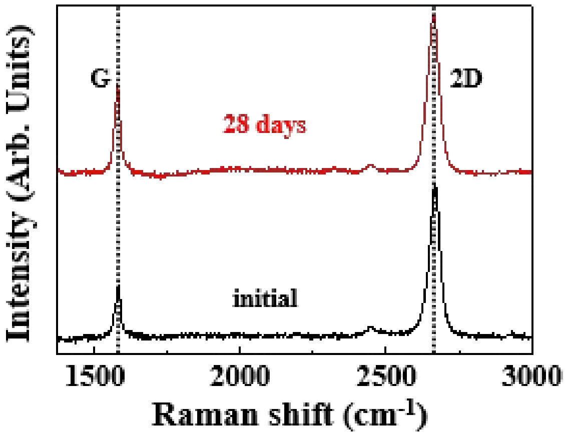

Fig. S7 Raman spectra of the graphene channel measured immediately and 28 days after the device fabrication.

References

[1] I. Vurgaftman, J.R. Meyer and L.R. Ram-Mohan, Band parameters for III–V compound semiconductors and their alloys, *J. Appl. Phys.*, 89 (2001) 5815-5875.

[2] K. Roy, M. Padmanabhan, S. Goswami, T.P. Sai, G. Ramalingam, S. Raghavan and A. Ghosh, Graphene–MoS2 hybrid structures for multifunctional photoresponsive memory devices, *Nat. Nanotechnol.*, 8 (2013) 826-830.

[3] X. Yang, C.-J. Wang, S. Cheng, X.-G. Yang, J.-H. Zang, C.-X. Shan, An ultraviolet-visible distinguishable broadband photodetector based on the positive and negative photoconductance effects of a graphene/ZnO quantum dot heterostructure, *Microstructures*, 3 (2023) N/A-N/A.

[4] L. Tao, Z. Chen, X. Li, K. Yan and J.-B. Xu, Hybrid graphene tunneling photoconductor with interface engineering towards fast photoresponse and high responsivity, *npj 2D Mater. Appl.*, 1 (2017) 19.

[5] A.C. Ferrari, D.M. Basko, Raman spectroscopy as a versatile tool for studying the properties of graphene, *Nat. Nanotechnol.*, 8 (2013) 235-246.

[6] L.G. Cançado, A. Jorio, E.M. Ferreira, F. Stavale, C.A. Achete, R.B. Capaz, M.d.O. Moutinho, A. Lombardo, T. Kulmala, A.C. Ferrari, Quantifying defects in graphene via Raman spectroscopy at different excitation energies, *Nano Lett.*, 11 (2011) 3190-3196.